Efficient Aeroelastic Analysis of Helicopter Blades via GNAT-based Model-Order Reduction Approach

Inho Jeong, Jeonbuk National University, Jeon-ju, Republic of Korea
Seung-Hoon Kang, Seoul National University, Seoul, Republic of Korea
Haedong Kim, Sejong University, Seoul, Republic of Korea
Haeseong Cho, Jeonbuk National University, Jeon-ju, Republic of Korea

Abstract

A model order reduction technique based on Proper Orthogonal Decomposition (POD) and Gauss-Newton with Approximated Tensors (GNAT) was applied to investigate the aeroelastic behavior of composite rotor blades. Rotor blades are slender and require aeroelastic analysis to accurately predict their response and the relevant vibratory loads, which involves numerous iterative calculations. To address this issue, the GNAT-based model order reduction (MOR) approach was applied to the geometrically exact beam theory. At this point, a low-dimensional approximation of the nonlinear finite element matrix of the system was constructed. The method was then applied to the aeroelastic analysis of a rotor blade. The results of the analysis demonstrate that the GNAT-based MOR can accurately capture the dynamics of these complex systems, while significantly reducing the computational cost. This approach has potential applications in the design and analysis of aerospace structures and systems, particularly those with geometrical nonlinearity and significant rotating effect.

1. NOTATION

Symbols

Geometrically exact beam theory:

a	Rotating reference frame
b	Rotating undeformed frame
B	Rotating deformed frame
t_1, t_2	Arbitrary fixed times
K	Kinetic energy density per unit length
U	Strain energy density per unit length
$\overline{\delta A}$	Virtual action of the beams end over the time interval
$\overline{\delta W}$	Virtual work resulting from applied loads per unit length
γ	Engineering force strain
κ	Engineering moment strain
V	Relative velocity, m/s
Ω	Angular velocity, rad/s
u	Displacement vector, m
ψ	Rotation vector, rad
v	Initial velocity, m/s
ω	Initial angular velocity, rad/s
C	Rotation matrix
C^{Ba}	Rotation matrix transforming vectors to deformed frame from reference frame
C^{ab}	Rotation matrix transforming vectors to reference frame from undeformed frame
C^{ba}	Rotation matrix transforming vectors to undeformed frame from reference frame
P	Linear momentum, kg-m/s
H	Angular momentum, kg-m^2/s
F	Internal force, N
M	Internal moment, N-m
M_{mass}	Mass matrix
S	Stiffness matrix
F_s	Structural operator
F_L	Lift operator
X	Structural operator
λ_{eigen}	Eigenvalue, rad/s
K_{spring}	Hinge stiffness
R	Force residual vector

$(\cdot)_a$	Quantity referring to the rotating reference frame
$(\cdot)_b$	Quantity referring to the rotating undeformed frame
$(\cdot)_B$	Quantity referring to the rotating deformed frame
$\widetilde{\widetilde{(\cdot)}}$	Convert a vector into a dual matrix
$(\cdot)^*$	Quantity satisfying geometrically exact relation
$\widetilde{(\cdot)}$	Boundary values of the corresponding quantities

Blade element theory:

V_∞	Relative speed in the inertial frame, m/s
$\lambda_{induced}$	Induced inflow coefficient
C^{ai}	Rotation matrix transforming vectors to reference frame from inertial frame
R_{radius}	Radius of rotor, m
C_T	Thrust coefficient of rotor
α	Angle of attack, deg
ρ	Density, kg/m^3
c	Chord length, m
c_l	Lift coefficient
c_d	Drag coefficient
c_m	Pitching moment coefficient
ϕ	Inflow angle, deg

Model order reduction:

q	Solution value
N	Degree of freedom of full-order model
S	Number of snapshots generated for the parameter
μ	Parameter of model
N_S	Total number of snapshots
$\boldsymbol{\Phi}$	Left singular matrix
$\boldsymbol{\Lambda}$	Right singular matrix
$\hat{\boldsymbol{u}}$	Solution vector
$\boldsymbol{T}_m$	POD mode from residual force vector
$\widehat{(\cdot)}$	Components of the reduced-order representation
$\widetilde{(\cdot)}$	Approximated representation
$(\cdot)^\dagger$	Moore-Penrose pseudo-inverse

Supplementary symbols:

n	Number of displacement bases
m	Number of residual bases
θ_o	Collective pitch angle, deg
σ	Rotor solidity
$(\cdot)_{FOM}$	Quantity of full-order model
$(\cdot)_{ROM}$	Quantity of reduced-order model

Acronyms:

POD	Proper Orthogonal Decomposition
GNAT	Gauss-Newton with Approximated Tensors
ROM	Reduced Order Model
FOM	Full Order Model
DEIM	Discrete Empirical Interpolation Method
MOR	Model Order Reduction
SVD	Singular Value Decomposition
GEBT	Geometrically Exact Beam Theory

2. INTRODUCTION

Rotor blade structural analysis relies heavily on two primary theories: the moderately large deformation beam theory (Ref. 1) and the geometrically exact beam theory (Ref. 2). The moderately large deformation beam theory is a displacement-based approach employed in structural models like the University of Maryland Advanced Rotorcraft Code (UMARC) (Refs. 3-4) and the Rotorcraft Comprehensive Analysis System (RCAS) (Ref. 5). On the other hand, the geometrically exact beam theory offers an advanced method to model slender structures, accounting for large displacements and rotations, thus providing more precise predictions of blade behavior under operational conditions. This theory has been implemented in rotorcraft comprehensive analysis (Ref. 6) and rotorcraft analysis codes such as DYnamic MOdal Reissner (DYMORE) (Ref. 7) and Comprehensive Analytical Model of Rotorcraft Aerodynamics and Dynamics (CAMRADII) (Refs. 8-9), including RCAS.

While the geometrically exact beam theory facilitates comprehensive structural analyses, it necessitates increased computational resources due to a higher degree of freedom in the system matrix. To mitigate these computational challenges, researchers have investigated reduced-order model (ROM) techniques to reduce system dimensionality while preserving key structural features. The Galerkin projection method (Ref. 10), a popular ROM technique, has been effectively used in various fields, including optimal control, structural dynamics, fluid dynamics, aeroelasticity, and fluid-structure interaction (FSI) (Refs. 11-16). However, when dealing with structural nonlinearity, the computational complexity of evaluating nonlinear terms remains comparable to that of the high-dimensional full-order model (FOM).

To address this, several methods have been proposed, such as the empirical interpolation method (EIM) (Ref. 17) and its variant, discrete EIM (DEIM)

(Ref. 18), which approximate nonlinear functions using separable interpolation functions. Additionally, the energy-conserving sampling and weighting (ECSW) method introduced by Farhat et al. (Ref. 19) offers a stable approach for approximating reduced nonlinear terms while maintaining numerical stability.

However, these reduction methods may face limitations with the geometrically exact beam theory due to the potential lack of symmetry in the system approximation matrix. The Gauss-Newton with approximated tensors (GNAT) method (Refs. 20-21) provides a promising alternative by enabling efficient evaluation of nonlinear terms through a Petrov–Galerkin projection associated with residual minimization. This method captures essential nonlinear features of the rotor blade system through selective sampling and interpolation techniques.

This study proposes a novel approach to the MOR of the geometrically exact beam theory based on a mixed variational formulation, utilizing the GNAT-based MOR. This approach aims to accurately model geometric nonlinearities in rotor blades while predicting internal forces efficiently. The proposed method's accuracy and computational efficiency are demonstrated through an aeroelastic trim analysis of a hingeless rotor under hovering flight conditions.

3. AERO-STRUCTURE COUPLED ANALYSIS

3.1. Geometrically exact beam theory

The mixed variational formulation based on the geometrically exact beam theory, derived from Hamilton's principle, is presented in Eq. (1).

$$\int_{t_1}^{t_2}\int_0^l \left[\delta(K-U)+\overline{\delta W}\right]dx_1dt = \overline{\delta A}. \tag{1}$$

The geometrically exact equations, formulated in the local reference frame, are presented in Eq. (2).

$$\begin{gathered}\gamma^* = C^{Ba}(C^{ab}e_1+u_a')-e_1.\\ \kappa^* = C^{ba}T_s(\theta)\theta',\\ V_B^* = C^{Ba}\left(v_a+\dot{u}_a+\tilde{\omega}_a u_a\right)-e_1,\\ \Omega_B^* = C^{ba}T_s(\theta)\dot{\theta}+C^{Ba}\omega_a.\end{gathered} \tag{2}$$

To establish a mixed variational formulation, Lagrange multipliers are employed to satisfy the geometrically exact equations.

$$\begin{gathered}\int_{t_1}^{t_2}\int_0^l [\delta V_B^{*T}P_B+\delta\Omega_B^{*T}H_B-\delta\gamma^{*T}F_B\\ -\delta\kappa^{*T}M_B+\delta F_B^T(\gamma-\gamma^*)+\delta M_B^T(\kappa-\kappa^*)\\ -\delta P_B^T(V_B-V_B^*)-\delta H_B^T(\Omega_B-\Omega_B^*)]dx_1dt\\ +\int_{t_1}^{t_2}\int_0^l\overline{\delta W}dx_1dt=\delta A.\end{gathered} \tag{3}$$

After integrating according to the transformation and eliminating all unknown spatial derivatives, we derive a mixed variational formulation in the rotating reference frame based on the fundamental and geometrically exact equations governing the dynamics of the moving beam, as follows:

$$\int_{t_1}^{t_2}\delta\Pi_a dt = 0. \tag{4}$$

The constitutive law, defined in Eq. (5), establishes the relationship between deformation and force, as well as between velocity and momentum.

$$\begin{Bmatrix}F_B\\ M_B\end{Bmatrix}=[S]\begin{Bmatrix}\gamma\\ \kappa\end{Bmatrix},\begin{Bmatrix}P_B\\ H_B\end{Bmatrix}=[M_{mass}]\begin{Bmatrix}V_B\\ \Omega_B\end{Bmatrix} \tag{5}$$

In Eq. (5), S represents the 6×6 stiffness matrix, where M_{mass} represents the 6×6 mass matrix. When Eq. (4) contains N elements, it can be represented as follows:

$$\int_{t_1}^{t_2}\delta\Pi_a dt = 0. \tag{6}$$

By employing a shape function and the relevant approximation [22], Eq. (6) can be expressed as

$$\int_{t_1}^{t_2}\delta X^T\left[F_s\left(X,\dot{X}\right)-F_L\left(X,\dot{X}\right)\right]dt=0, \tag{7}$$

where F_s represents the structural operator, F_L is the lifting operator, and X is the structural state variable. The structural state variables comprise the displacement, rotation, internal force, internal moment, linear momentum, and angular momentum of the beam elements and can be expressed as Eq. (8).

$$\begin{gathered}X=[\check{F}_1^T\ \check{M}_1^T\ u_1^T\ \theta_1^T\ F_1^T\ M_1^T\ P_1^T\ H_1^T\ \ldots\\ u_N^T\ \theta_N^T\ F_N^T\ M_N^T\ P_N^T\ H_N^T\ \check{u}_{N+1}^T\check{\theta}_{N+1}^T].\end{gathered} \tag{8}$$

In summary, the equations can be consolidated and represented as shown in Eq. (9).

$$F_s\left(X,\dot{X}\right)-F_L\left(X,\dot{X}\right)=0 \tag{9}$$

The Jacobian of the structural operator is given by Eq. (10).

$$\left[\frac{\partial F_S}{\partial X}\right]X + \left[\frac{\partial F_S}{\partial \dot{X}}\right]\dot{X} = 0, \tag{10}$$

where the Jacobian of the structural operator is assembled as $\frac{\partial F_S}{\partial X} = \sum_i \left(\frac{\partial F_S}{\partial X}\right)_i$, and each component $\left(\frac{\partial F_S}{\partial X}\right)_i$ is as follows:

$$\frac{\partial F_S}{\partial X_i} = \begin{bmatrix} 0 & \frac{\partial f_{u_i}}{\partial \theta} & \frac{\partial f_{u_i}}{\partial F} & 0 & \frac{\partial f_{u_i}}{\partial P} & 0 \\ 0 & \frac{\partial f_{\psi_i}}{\partial \theta} & \frac{\partial f_{\psi_i}}{\partial F} & \frac{\partial f_{\psi_i}}{\partial M} & \frac{\partial f_{\psi_i}}{\partial P} & \frac{\partial f_{\psi_i}}{\partial H} \\ \frac{\partial f_{F_i}}{\partial u} & \frac{\partial f_{F_i}}{\partial \theta} & \frac{\partial f_{F_i}}{\partial F} & \frac{\partial f_{F_i}}{\partial M} & 0 & 0 \\ 0 & \frac{\partial f_{M_i}}{\partial \theta} & \frac{\partial f_{M_i}}{\partial F} & \frac{\partial f_{M_i}}{\partial M} & 0 & 0 \\ \frac{\partial f_{P_i}}{\partial u} & \frac{\partial f_{P_i}}{\partial \theta} & 0 & 0 & \frac{\partial f_{P_i}}{\partial P} & \frac{\partial f_{P_i}}{\partial H} \\ 0 & \frac{\partial f_{H_i}}{\partial \theta} & 0 & 0 & \frac{\partial f_{H_i}}{\partial P} & \frac{\partial f_{H_i}}{\partial H} \\ 0 & \frac{\partial f_{u_j}}{\partial \theta} & \frac{\partial f_{u_j}}{\partial F} & 0 & \frac{\partial f_{u_j}}{\partial P} & 0 \\ 0 & \frac{\partial f_{\psi_j}}{\partial \theta} & \frac{\partial f_{\psi_j}}{\partial F} & \frac{\partial f_{\psi_j}}{\partial M} & \frac{\partial f_{\psi_j}}{\partial P} & \frac{\partial f_{\psi_j}}{\partial H} \\ \frac{\partial f_{F_j}}{\partial u} & \frac{\partial f_{F_j}}{\partial \theta} & \frac{\partial f_{F_j}}{\partial F} & \frac{\partial f_{F_j}}{\partial M} & 0 & 0 \\ 0 & \frac{\partial f_{M_j}}{\partial \theta} & \frac{\partial f_{M_j}}{\partial F} & \frac{\partial f_{M_j}}{\partial M} & 0 & 0 \end{bmatrix}. \tag{11}$$

The static response analysis follows the procedure depicted in Fig. 1.

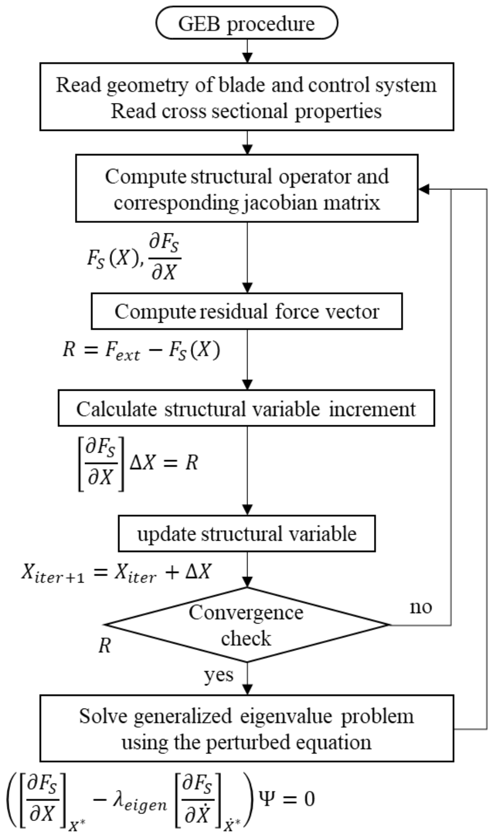

Figure 1: Static analysis procedure of geometrically exact beam theory

The process begins by calculating the load residual using the Newton-Raphson method, tailored specifically for the structural operator in question. Next, the Jacobian of the structure and the load residual are used to determine the incremental change in the structural state variable, which is then updated. This iterative process continues until the load residual reaches the specified tolerance. Once this convergence criterion is met, the analysis is deemed complete and may proceed to the next step, which could involve incrementally increasing the load or conducting a new analysis under different conditions. To ensure solution stability, it is often necessary to apply the load incrementally rather than in a single step, as is commonly done in such analyses.

3.2. Newmark-β method

Dynamic analysis based on the geometrically exact beam theory uses the Newmark-β method. In dynamic response analysis, the results from static response analysis, which reflect the rotational effects, serve as initial values to accurately capture the rotor's rotation. The initial values at each time step are as follows:

$$\begin{gathered} X_t = X_{t-1} \\ \ddot{X}_t = \frac{1}{\beta \Delta t^2}\Delta X - \frac{1}{\beta \Delta t}\dot{X}_{t-1} - \frac{0.5-\beta}{\beta}\ddot{X}_{t-1} \\ \dot{X}_t = \dot{X}_{t-1} + \Delta t((1-\gamma)\ddot{X}_{t-1} + \gamma \ddot{X}_{t-1}) \end{gathered} \tag{12}$$

The effective jacobian of the structural operator is expressed as follows:

$$\frac{\partial F_S}{\partial X}_{eff} = \frac{\partial F_S}{\partial X}^n + \frac{1}{\beta \Delta t}\frac{\partial F_S}{\partial \dot{X}}^n \tag{13}$$

The structural variable is determined using the Newton-Raphson method.

$$\begin{gathered} \left[\frac{\partial F_S}{\partial X}_{eff}\right]\Delta X = \Delta R \\ \Delta R = F_L(X, \dot{X}) - F_S(X) \end{gathered} \tag{14}$$

The dynamic analysis procedure is illustrated in Fig. 2. It follows a similar process to the static analysis, but with the effective Jacobian. The primary difference is that the time derivatives (first and second derivatives) of the solution are computed using the Newmark-β method.

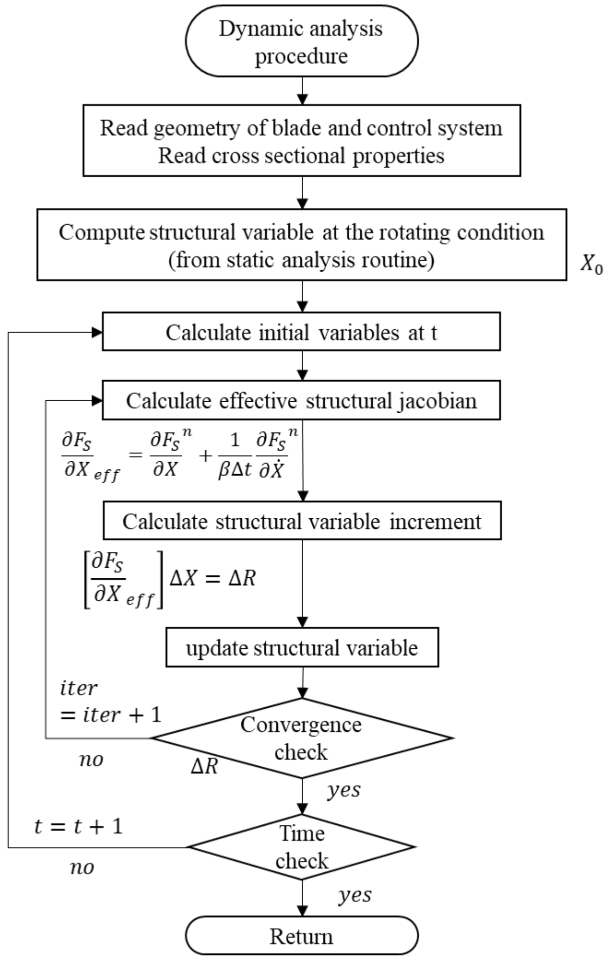

Figure 2: Dynamic analysis procedure of geometrically exact beam theory

3.3. Multi-body modeling

The rotor comprises several components, including blades, pitch bearings, and hinges, making multi-body modeling essential for accurate response analysis. In this study, multi-body modeling is performed using the penalty method. This approach allows for the modeling of various joints required for the rotor hub, such as revolute, universal, and spherical joints. To impose constraints between two independent bodies in the penalty method, a force is applied to satisfy the specified constraint.

$$\begin{aligned} F_{penalty} &= K_i^u \times (u_2 - u_1 - u_{control}) \\ M_{penalty} &= K_i^\theta \times (\theta_2 - \theta_1 - \theta_{control}) \end{aligned} \tag{15}$$

When applying the penalty method to elements 1 and 2, a penalty term is added to the Jacobian at the nodes where the constraints are enforced. In the geometrically exact beam theory based on the mixed variational formulation, both the displacement and rotation of elements are calculated. If the difference between the current displacement and rotation and the desired control input is zero, no load is applied. However, if there is a discrepancy, a load is applied proportional to the magnitude of the difference and the stiffness, ensuring that the desired connection conditions are met.

3.4. Blade element theory for aerodynamic loads

The relative speed in the rotating deformed frame is given by Eq. (16).

$$U_B = C^{Ba}(C^{ai}V_\infty + \lambda_{induced} e_3) \tag{16}$$

The induced inflow velocity perpendicular to the rotor plane is calculated using the uniform inflow assumption.

$$\lambda_{induced} = \Omega R_{radius} \sqrt{\left(\frac{C_T}{2}\right)}, \tag{17}$$

The aerodynamic loads, derived using the blade element method, are determined by Eq. (18).

$$\begin{aligned} dL &= \frac{1}{2}\rho c_l(\alpha_B) c U_B^2 dy, \\ dD &= \frac{1}{2}\rho c_d(\alpha_B) c U_B^2 dy, \\ dM &= \frac{1}{2}\rho c_m(\alpha_B) c^2 U_B^2 dy, \\ \alpha_B &= -\phi_B. \end{aligned} \tag{18}$$

The aerodynamic loads f_{wind} with respect to the wind axis and the geometrically exact beams use the loads f_a with respect to the rotating reference frame. Therefore, the loads in the rotating reference frame can be obtained through a coordinate transformation.

$$\begin{aligned} f_a &= C^{ab} C^{bB} C^{\phi_B} f_{wind}, \\ f_{wind} &= [0,\ -dD,\ dL]^T \end{aligned} \tag{19}$$

3.5. Aeroelastic trim analysis

The trim analysis procedure for hovering conditions is illustrated in Fig. 3. To estimate the rotor thrust and determine the necessary collective pitch angle to achieve the desired hover thrust, structural and aerodynamic models are coupled. An optimization approach is used to adjust the collective pitch angle to meet the target thrust coefficient. Auto-pilot is employed for the present trim analysis.

Aerodynamic loads and performance coefficients are calculated while accounting for structural deformation. These loads are then applied to the structural analysis by transforming them into loads acting on the structural nodes. The resulting structural deformation is then used to update the aerodynamic analysis. This process is iterated until convergence is achieved through a coupled aerodynamic-structural analysis. The trim analysis continues by adjusting the collective pitch until the target thrust coefficient is attained.

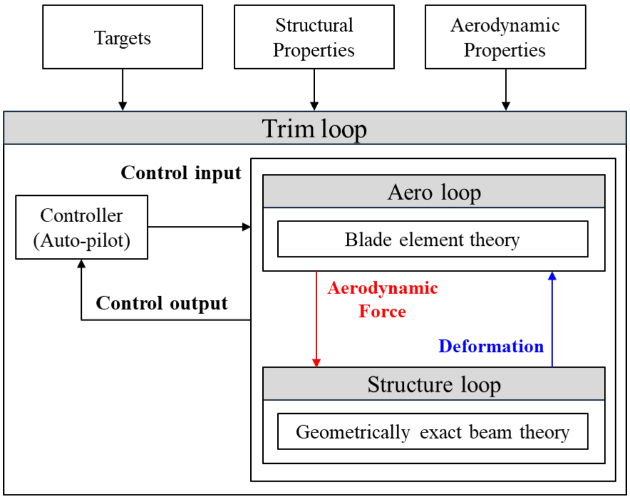

Figure 3: Trim analysis procedure through aero-structure coupled analysis

4. MODEL-ORDER REDUCTION

As discussed earlier, rotor blade aeroelastic analysis requires numerous iterative calculations. To enhance computational efficiency while maintaining accuracy, especially during trim analysis and optimization under various operating conditions, this study employs a GNAT-based MOR applied to the geometrically exact beam theory. The GNAT-based MOR is a projection-based model reduction technique that reduces the dimensionality of the governing equations, thereby lowering computational costs.

In the offline phase, the FOM is evaluated under different conditions to extract the reduced bases. During the online phase, the ROM is constructed by incorporating these reduced-order bases along with nonlinear terms at each iteration step. The relevant formulations for the ROM techniques are detailed in the following subsections.

4.1. Proper Orthogonal Decomposition

ROMs are constructed based on data obtained from FOM analysis. This involves collecting solutions from the FOM, which are compiled into a "snapshot matrix." In this context, q represents a solution from the FOM analysis, N indicates the degrees of freedom in the FOM, S is the number of snapshots generated for each parameter μ, and N_s denotes the total number of snapshots.

$$\boldsymbol{W} = \begin{bmatrix} q_1^{(1,1)} & \cdots & q_1^{(S_1,1)} & q_1^{(1,2)} & \cdots & q_1^{(S_2,2)} & q_1^{(1,\mu)} & \cdots & q_1^{(S_\mu,\mu)} \\ \vdots & \ddots & \vdots & \vdots & \ddots & \vdots & \vdots & \ddots & \vdots \\ q_N^{(1,1)} & \cdots & q_N^{(S_1,1)} & q_N^{(1,2)} & \cdots & q_N^{(S_2,2)} & q_N^{(1,\mu)} & \cdots & q_N^{(S_\mu,\mu)} \end{bmatrix} \in \mathbb{R}^{N\times N_s} \tag{20}$$

Using Algorithm 1, orthogonal basis vectors that represent the system characteristics are extracted from the snapshot matrix. The process begins by inputting the snapshot matrix derived from the FOM. Singular value decomposition (SVD) is then applied to this matrix to identify these basis vectors.

$$\begin{gathered} \boldsymbol{W} = \boldsymbol{\Phi\Sigma\Lambda^T}, \boldsymbol{\Phi} \in \mathbb{R}^{N\times N_s}, \\ \boldsymbol{\Sigma} = diag(\sigma_1, \ldots, \sigma_{N_s}), and\ \boldsymbol{\Lambda^T} \in \mathbb{R}^{N_s\times N_s} \end{gathered} \tag{21}$$

The complete set of POD basis vectors, denoted as $\boldsymbol{V}$, is composed of the first n column vectors from the left singular matrix $\boldsymbol{\Phi}$ obtained from the SVD.

Algorithm 1 POD basis computation
Input : Snapshot matrix $\boldsymbol{W} \in \mathbb{R}^{N\times N_s}$
Output : POD basis $\boldsymbol{V} \in \mathbb{R}^{N\times n}$
1: Compute the thin SVD: $\boldsymbol{W} = \boldsymbol{\Phi\Sigma\Lambda^T}$
2: Select the dimension of POD basis, n
3: Construct $\boldsymbol{V}$ using selected POD basis vectors
$\boldsymbol{v} = [\boldsymbol{\phi}_1, \ldots, \boldsymbol{\phi}_n]$

4.2. Galerkin-projection with permuted modes

To define the ROM, a nonlinear equation is projected onto the reduced space via Galerkin projection. When using geometrically exact beam theory based on the mixed variational formulation, internal force and momentum are derived in addition to displacement in the structural variable $\boldsymbol{X}$. Thus, if $\boldsymbol{V}$ is used itself, performance may be limited by the discontinuity of each variable. Therefore, $\boldsymbol{V}$ can be expressed as follows so that the same variables are considered during the dimensional reduction process.

$$\boldsymbol{V_P} = \begin{bmatrix} \phi_1^{(u_1,\theta_1)} \cdots \phi_n^{(u_1,\theta_1)} & & & \\ & \phi_1^{(F_1,M_1)} \cdots \phi_n^{(F_1,M_1)} & & \\ & & \cdots & \\ & & & \phi_1^{(P_N,H_N)} \cdots \phi_n^{(P_N,H_N)} \end{bmatrix} \in \mathbb{R}^{N\times(N\times n)} \tag{22}$$

By applying the Galerkin projection to the governing equations, the solution in the entire dimension and the solution in the reduced dimension can be expressed as follows.

$$\boldsymbol{X}(\boldsymbol{\mu}) = \boldsymbol{V_P}\hat{\boldsymbol{X}}(\mu) \tag{23}$$

The approximated Jacobian and residuals at the k-th step derived through POD-Galerkin projection are as follows.

$$\frac{\partial \widehat{F_S}}{\partial X}^k = {V_P}^T \frac{\partial F_S}{\partial X}(V_P\widehat{X}(\mu);\mu)V_P, \tag{24}$$

$$\hat{r}^k = {V_P}^T r(V_P\widehat{X}(\mu);\mu) \tag{25}$$

4.3. Gauss-Newton with Approximation Tensor

If hyper reduction is applied to the ROM for nonlinear analyis, sparse sampling can be employed to approximate the nonlinear functions. In the case of POD-GNAT, DEIM indices and nonlinear least square are applied while utilizing the existing POD bases.

$$\Delta\widehat{X} = \arg\min\left\|\frac{\partial F_S}{\partial X}(V\widehat{X}(\mu);\mu)V\mathbf{z} - r(V\widehat{X}(\mu);\mu)\right\|_2. \tag{26}$$

The matrix P is constituted by a set of m vectors, denoting the DEIM indices to approximate the nonlinear terms. .

$$P = \left[e_{p_1}, \dots, e_{p_m}\right] \in \mathbb{R}^{N\times m} \tag{27}$$

where e_{p_m} represents the p_m-th column of an $N \times N$ identity matrix. Consequently, the hyper-reduction for the residual force vector and the Jacobian matrix is accomplished. Summary of computing the DEIM indices is summarized in Algorithm 2.

Algorithm 2 Compute the DEIM indices

Input : POD basis $T_m = [t_1, \dots, t_m]$
Output : Interpolation indices $p_m = [p_1, \dots, p_m]$
procedure DEIM
  set $p_1 = maxloc\{t_1\}$
  $T_m = [t_1], P = [e_{p_1}]$
  for $k = 2$ to m **do**
    solve $c = (P^T T_m)^{-1} P^T t_k$
    $w = t_k - T_m c$
    $p_k = maxloc\{w\}$
    $T_m \leftarrow [T_m\ t_k], P \leftarrow [P\ e_{p_k}]$
    end for
end procedure

The ROM at the kth iteration can be expressed as

$$\frac{\partial \widehat{F_S}}{\partial X}^k = (P^T T_m)^\dagger P^T \frac{\partial F_S}{\partial X}(V\widehat{X}(\mu);\mu), \tag{28}$$

$$\hat{r}^k = (P^T T_m)^\dagger P^T r(V\widehat{X}(\mu);\mu) \tag{29}$$

where † denotes the Moore–Penrose pseudo-inverse. The relevant solution based on the Gauss-Newton problem results in the following Eq. (30).

$$\Delta\widehat{X} = \arg\min\left\|(P^T T_m)^\dagger P^T \frac{\partial F_S}{\partial X}(V\widehat{X}(\mu);\mu)V\mathbf{z} - (P^T T_m)^\dagger P^T r(V\widehat{X}(\mu);\mu)\right\|_2. \tag{30}$$

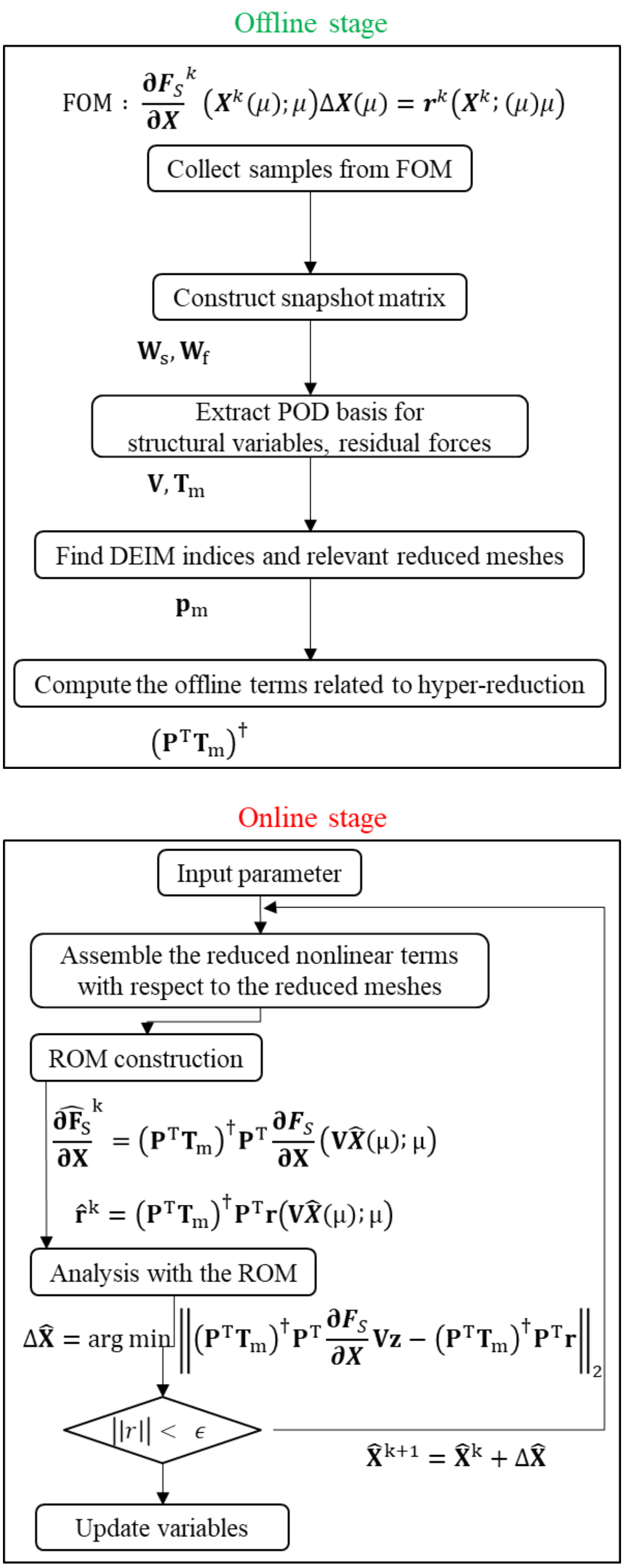

Figure 4: Proposed GNAT-based MOR for the GEBT

Figure 4 illustrates the application of POD-GNAT to the geometrically exact beam theory, comprising offline and online stages.

In the offline stage, the FOM for the geometrically exact beam theory is analyzed across various values of

μ, where μ may represent parameters such as the blade's collective pitch, load conditions, or material properties. From this analysis, structural state variables and force residuals are computed and used to construct the snapshot matrices $\boldsymbol{W}_s$ and $\boldsymbol{W}_f$, respectively. Algorithm 1 is then utilized to extract the basis vectors $\boldsymbol{V}$ and $\boldsymbol{T}_m$. Subsequently, Algorithm 2 is employed to compute the DEIM indices, which identify the locations of the reduced degrees of freedom. For efficiency, $(\boldsymbol{P}^T\boldsymbol{T}_m)^\dagger$, which is needed for repeated calculations during the online stage, is precomputed.

In the online stage, the precomputed terms are used to derive the Jacobian and residual in the reduced dimension, denoted as $\frac{\partial \widehat{\boldsymbol{F}_S}}{\partial \boldsymbol{X}}^k$ and $\hat{\boldsymbol{r}}^k$, respectively. The increment of structural state variables, $\Delta\widehat{\boldsymbol{X}}$, in the reduced dimension is calculated using Eq. (30).

5. NUMERICAL VERIFICATION

In this section, we present the results of the proposed GNAT-based MOR for the geometrically exact beam theory (POD-GNAT-GEBT) in the quasi-static aeroelastic analysis of a full-scale hingeless rotor blade. This analysis highlights the enhanced computational efficiency of the POD-GNAT-GEBT, given the higher degrees of freedom and increased computational demands associated with aeroelastic analysis. The first and second examples focus on hovering analysis and the corresponding trim analysis for hovering flight to demonstrate the improvements in computational efficiency provided by the POD-GNAT-GEBT.

To validate the proposed method, we compare the results obtained with POD-GNAT-GEBT to those from the FOM, DYMORE II, and CAMRAD II. Both DYMORE II and CAMRAD II utilize the geometrically exact beam theory (GEBT) and uniform inflow models for their analyses.

The rotor specifications used in these analyses are detailed in Table 1. Additionally, a speed-up factor is calculated to assess the efficiency of the POD-GNAT-GEBT. This factor is determined by dividing the CPU time required for the FOM analysis by the CPU time required for the POD-GNAT-GEBT analysis. A higher speed-up factor indicates a greater reduction in computational time.

(31) $$\text{Speed} - \text{up factor} = \frac{\text{CPU time for FOM}}{\text{CPU time for ROM}}.$$

Table 1: Full-scale hingeless rotor specifications.

Parameter	Value
Radius	4.91 m
Hub Offset	0.1473 m
Twist	4.238°(1.079m) -2.032°(tip)
Airfoil	NACA 23012
Rotor Speed	425 RPM
Number of Blades	4
Precone angle	2.5°

The assessment of the model's accuracy involves two accuracy factors, each normalized between 0 and 1. These factors are determined by comparing the results of the ROMs to those of the FOMs. Values closer to 1 indicate high accuracy in the comparisons.

The relative discrepancy of the displacement, as defined in [23], can be expressed as

(32) $$e_1 = \max\left(0, 1 - \frac{\sqrt{\Delta u^T \Delta u}}{\sqrt{u_{FOM}^T u_{FOM}^T}}\right),$$

where

$$\Delta u = u_{FOM} - u_{ROM}.$$

The relative discrepancy of the internal force and moment can be expressed as

(33) $$e_2 = \max\left(0, 1 - \frac{\left(\frac{\sqrt{\Delta F^T \Delta F}}{\sqrt{F_{FOM}^T F_{FOM}^T}} + \frac{\sqrt{\Delta M^T \Delta M}}{\sqrt{M_{FOM}^T M_{FOM}^T}}\right)}{2}\right),$$

Where,

$$\Delta F = F_{FOM} - F_{ROM}, \Delta M = M_{FOM} - M_{ROM}.$$

5.1. Aeroelastic analysis for prescribed collective pitch angle

The POD-GNAT-GEBT analysis for hovering flight conditions must accommodate variations in the collective pitch angle, θ_o. To cover the range of collective pitch angles, a hover aeroelastic analysis is performed for four specific angles: θ_o: 3°, 6°, 9°, and 12°. For validation, four cases are selected by incrementally increasing the collective pitch angle, with the angles as follows: Case 1: θ_o=3.54°, Case 2: θ_o=7.67°, Case 3: θ_o=10.82°, and Case 4: θ_o=13.45°. Cases 1–3 fall within the sampling range (interpolation), while Case 4 extends beyond this range (extrapolation).

In this study, 725 snapshots are generated, and the corresponding displacement and residual bases are derived. The POD-GNAT-GEBT is formulated by varying the number of displacement bases n from 20 to 90 and the number of residual bases m from 100 to 400. The overall accuracy is verified using the e_1 and e_2 accuracy metrics, considering the structural behavior of the full-scale hingeless blade.

The accuracy of the POD-GNAT-GEBT is confirmed for both Case 1 (within the sampling range) and Case 4 (outside the sampling range). Figure 5 illustrates the discrepancy in displacement for Cases 1 and 4. For e_1, Case 1 achieved accuracies ranging from 0.9 to 0.95, independent of the number of bases used. In Case 4, the accuracy ranged from 0.85 to 0.9 across all considered bases, with no clear dependence on the number of bases. Figure 6 shows the discrepancy in internal forces for Case 4, showing high accuracies of 0.95 or greater for all considered bases across all four cases.

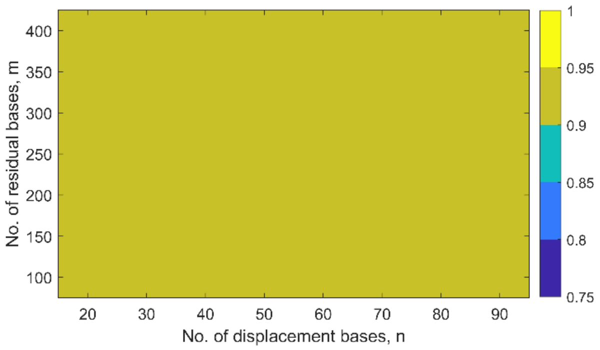

(a) Case 1 (θ_0= 3.54°)

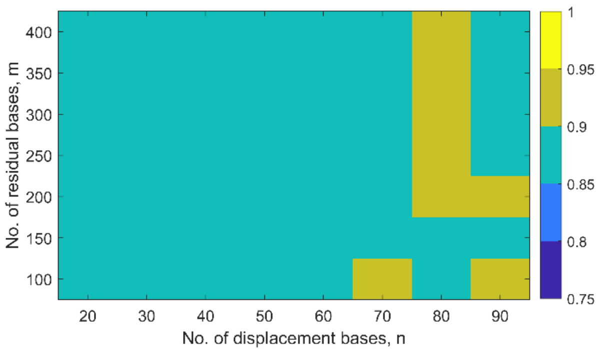

(b) Case 4 (θ_0= 13.45°)

Figure 5: Relative discrepancy of displacement of full-scale hingeless blade (e_1)

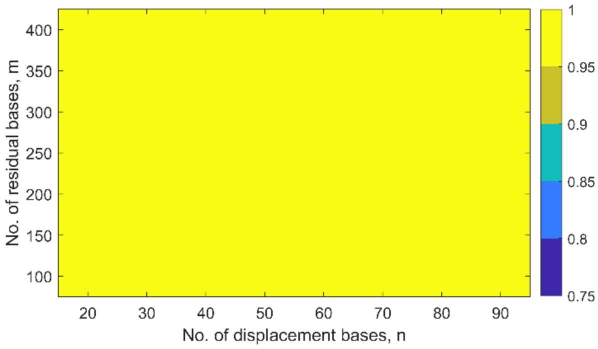

Case 4 (θ_0= 13.45°)

Figure 6: Relative discrepancy of internal force of full-scale hingeless blade (e_2)

Figure 7 shows the speed-up factors for Cases 1 and 4. It is observed that the speed-up factor degrades when the number of displacement and residual bases decreases. As the number of bases increases, the convergence characteristics improve, leading to fewer iterations required. This comparison underscores the importance of balancing accuracy with computational efficiency. In this study, a model utilizing 80 displacement bases and 200 residual bases is chosen for its effective balance between accuracy and speed-up factor.

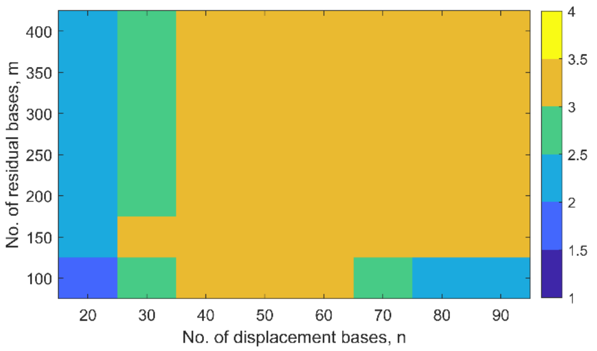

(a) Case 1 (θ_0= 3.54°)

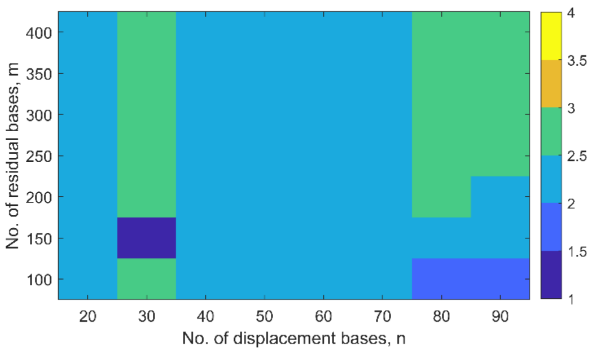

(b) Case 4 (θ_0= 13.45°)

Figure 7: Speed-up factor of displacement of full-scale hingeless blade.

For a model utilizing 80 displacement bases and 200 residual bases, the tip displacements and distribution of internal forces are compared with those from the FOM for each case. Figure 8 shows the flap/lag displacement and elastic twist at the tip for each case, demonstrating that these values closely match those from the FOM.

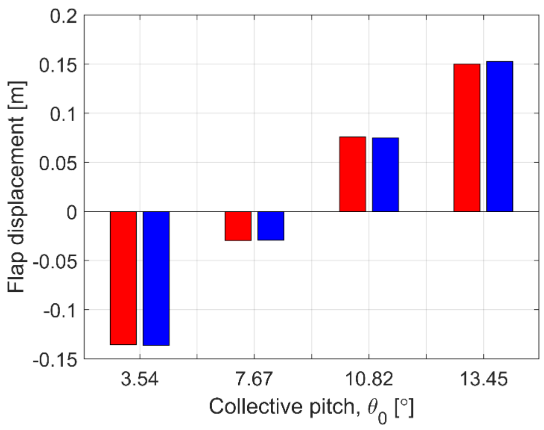

(a) Flap displacement

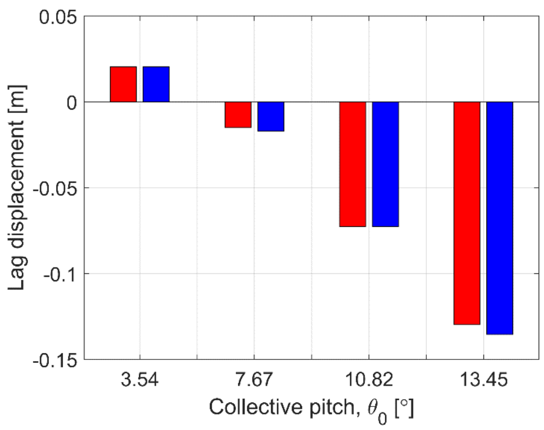

(b) Lag displacement

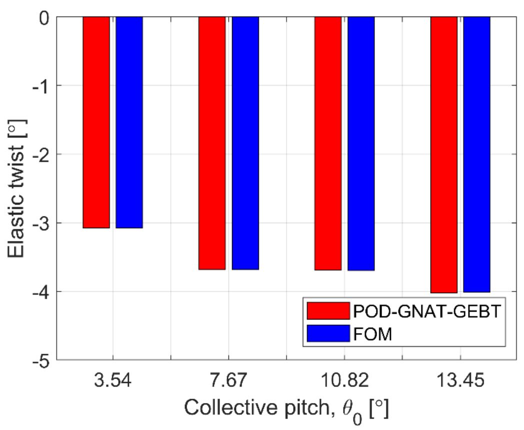

(c) Elastic twist

Figure 8: Tip displacement with respect to collective pitch of full-scale hingeless rotor blade.

Figure 9 illustrates the internal flap, lag, and torsion moments along the spanwise direction. The flap and torsion moments exhibit strong correlation with the FOM predictions. Consequently, the comparison of tip displacement and internal loads indicates that the POD-GNAT-GEBT delivers results with comparable accuracy to the FOM.

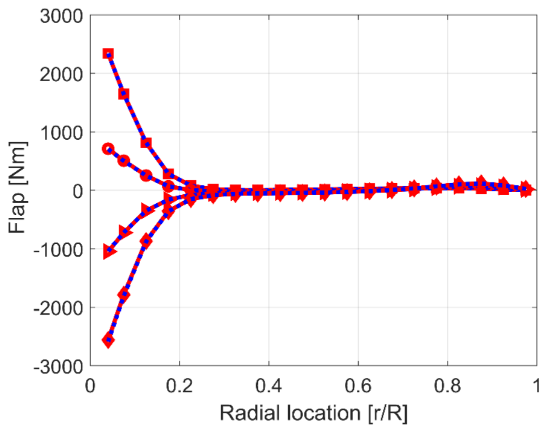

(a) Flapwise bending moment

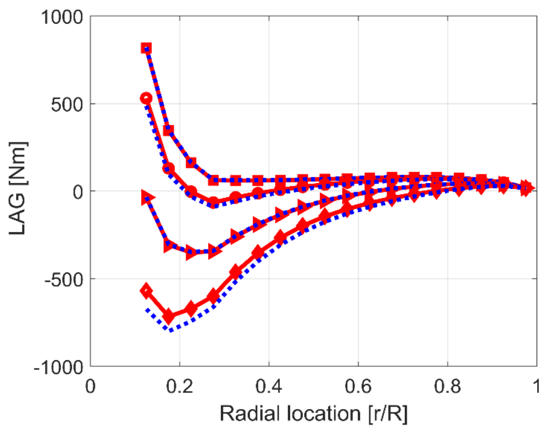

(b) Lagwise bending moment

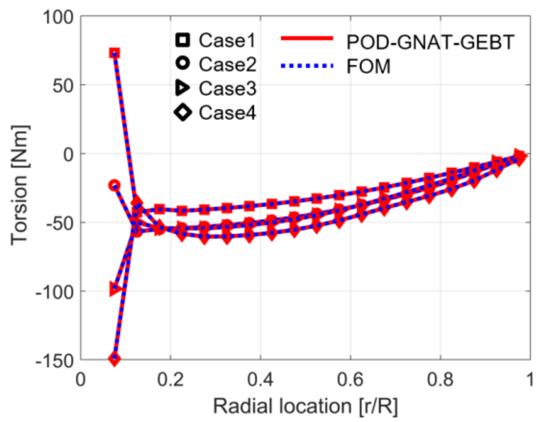

(c) Torsional moment

Figure 9: Spanwise internal force with respect to collective pitch of full-scale hingeless rotor blade.

Figure 10 shows a fan plot generated using POD-GNAT-GEBT with 80 displacement bases and 200 residual bases. The results are compared with those obtained from the FOM, CAMRAD II, and DYMORE II. It is confirmed that the results from POD-GNAT-GEBT closely match those from the FOM and exhibit similar trends when compared with CAMRAD II and DYMORE II.

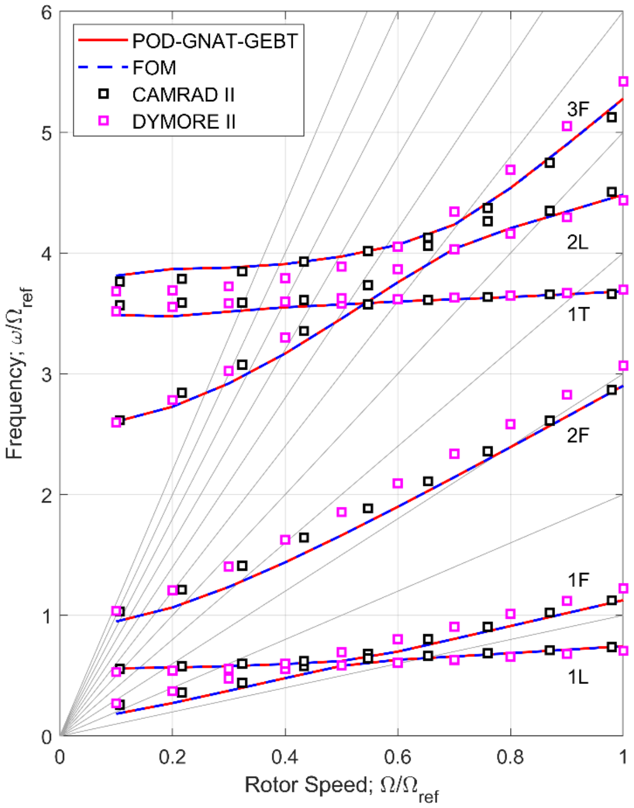

Figure 10: Fan plot of full-scale hingeless blade.

Subsequently, hover analyses are conducted using POD-GNAT-GEBT, taking into account the prescribed collective pitch angles. Figure 11 presents a comparison of the rotor thrust coefficient, power coefficient, and flapwise moment (FM) with NASA's experimental data [24]. This comparison highlights the effectiveness and accuracy of the proposed POD-GNAT-GEBT in performing precise and efficient aeroelastic hovering analyses.

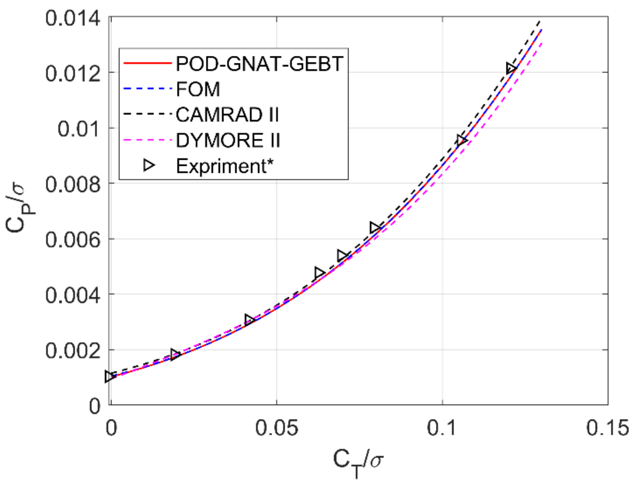

(a) Rotor power

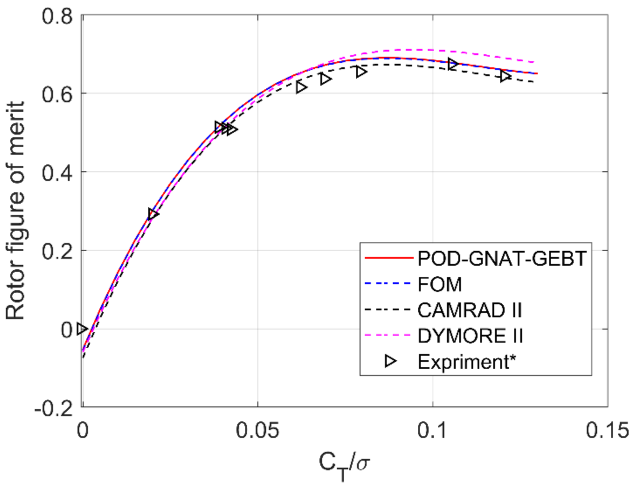

(b) Rotor figure of merit

Figure 11: Predicted rotor performance of full-scale hingeless rotor blade, 425RPM.

5.2. Trim analysis for hovering condition

The next step involved a trim analysis for hovering flight, which accounted for the thrust coefficient and its relation to inflow intensity. The primary variables considered in this trim analysis are the collective pitch angle and the target thrust coefficient relative to the inflow strength. For example, at the same collective pitch angle, a higher target thrust coefficient indicates stronger inflow, while a lower value signifies weaker inflow. Using Latin hypercube sampling, 24 sampling points are chosen for the collective pitch and target thrust coefficient (see Fig. 12). The corresponding calculations are performed to gather the snapshots, resulting in a snapshot matrix constructed from the 3,577 snapshots collected during the analysis.

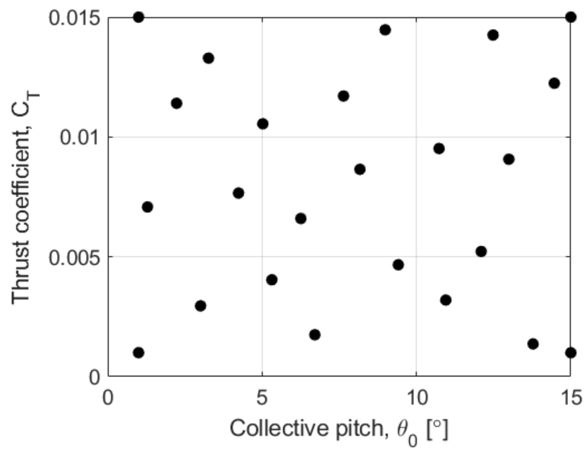

Figure 12: Sampling point with parameter variation for trim analysis of hovering state.

POD-GNAT-GEBT, utilizing 80 displacement bases (n) and 200 residual bases (m), is employed to conduct a trim analysis for hovering flight across four distinct conditions. Based on the sampling shown in Fig. 12, four trim targets C_T/σ for verification are selected: Case 1: $C_T/\sigma = 0.02$, Case 2: $C_T/\sigma = 0.06$, Case 3: $C_T/\sigma = 0.1$, Case 4: $C_T/\sigma = 0.13$

Figure 13 compares the collective pitch angles obtained from the hover-trim analysis across these various thrust conditions. The results from POD-GNAT-GEBT show close correlation with those from the FOM, CAMRAD II, and DYMORE II, with POD-GNAT-GEBT and FOM results being particularly well-aligned.

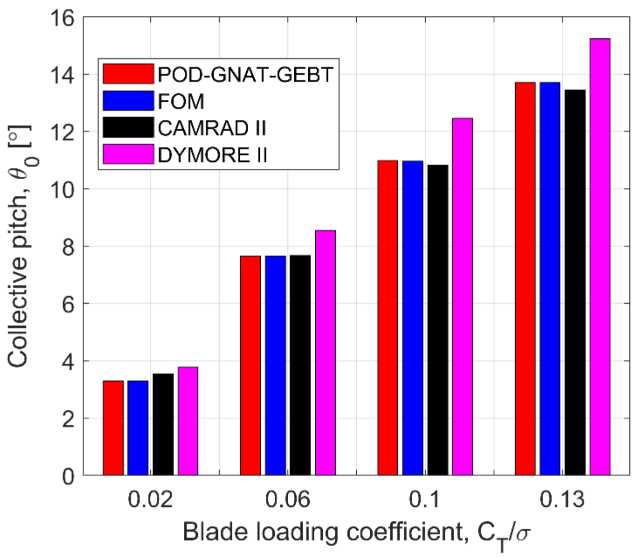

Figure 13: Collective pitch angle of each case calculated from trim analysis.

A summary of the online computation times under various thrust conditions is presented in Table 2, along with the corresponding speed-up factors. Case 1 achieved the highest speed-up factor of 1.91, while Case 3 showed the lowest speed-up factor of 1.69, indicating the least reduction in computational time efficiency.

Table 2: Computational cost and speed-up factor of each case for trim analysis.

	Case1	Case2	Case3	Case4
	Time [s]			
FOM	27.30	9.33	16.31	38.17
POD-GNAT-GEBT	14.00	5.30	9.67	20.18
	Speed-up factor			
	1.95	1.76	1.69	1.89

Figure 14 illustrates the time required for analysis based on the accumulated number of trim analyses. For POD-GNAT-GEBT, the offline stage takes 79 seconds to establish the model. Notably, when the number of analyses reaches 8 or more, the time required for ROM analysis is less than that for FOM analysis. This trend indicates that the speed-up factor continues to improve with a greater number of iterations in the trim analyses, demonstrating the enhanced computational efficiency of POD-GNAT-GEBT. Consequently, POD-GNAT-GEBT proves to be both accurate and efficient for trim analysis applications.

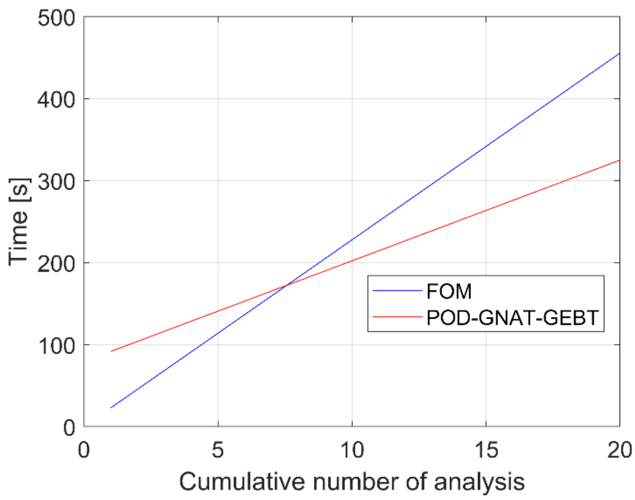

Figure 14: Comparison of FOM and POD-GNAT-GEBT computational cost.

5.3. Dynamic analysis

For the extension to dynamic analysis, HART-II rotor blade is considered. The relevant information is summarized in Table 3.

Table 3: Hingeless rotor specifications.

Parameter	Value
Radius	2 m
Hub Offset	0.075 m
Twist	4.24°(0.44m) -2°(tip)
Airfoil	NACA 23012
Rotor Speed	1041 RPM
Number of Blades	4
Precone angle	2.5°

Cyclic loads are applied to the blade's flap, lag direction load, and pitching moment. The relevant loading condition is depicted in Fig. 15.

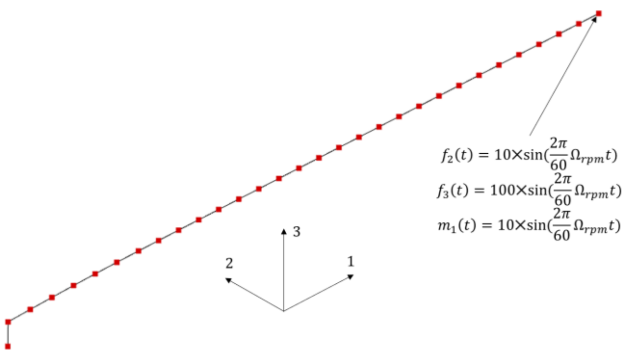

Figure 15: Tip displacement of HART-II blade.

To create the POD-GEBT model, dynamic analysis of FOM is performed for a total of 5 revolutions. Moreover, a snapshot matrix consisting of structural variables is obtained.

Consequently, POD-GEBT is created considering 20 permuted POD modes. The same load conditions are applied to 10 revolutions, twice the 5 revolutions used to sample the model. Figure 16 compares the tip displacements in the flap, lag, and twist between FOM and ROM.

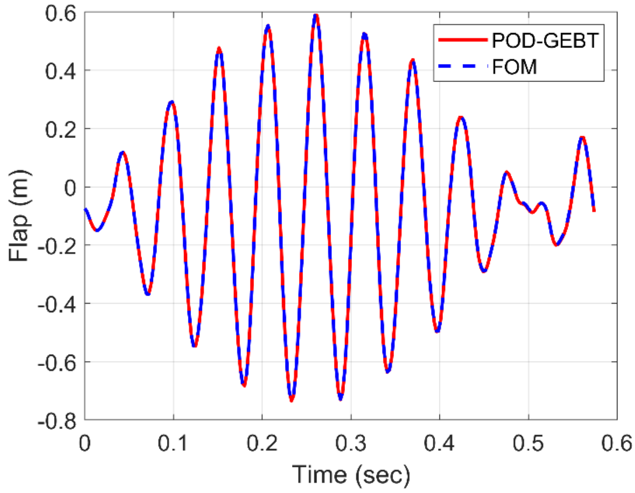

(a) Flap displacement of HART-II blade

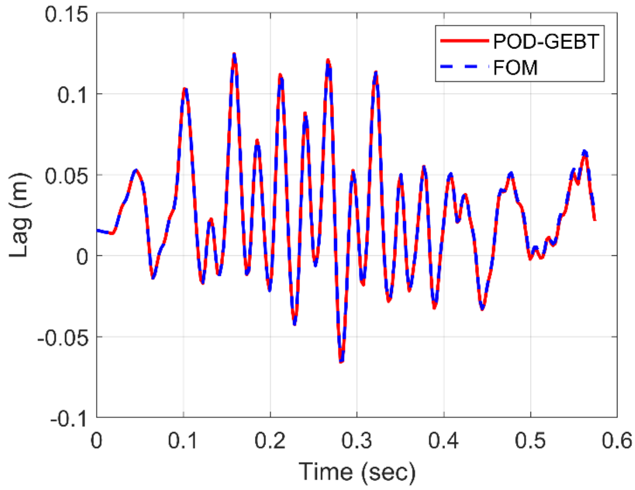

(b) Lag displacement of HART-II blade

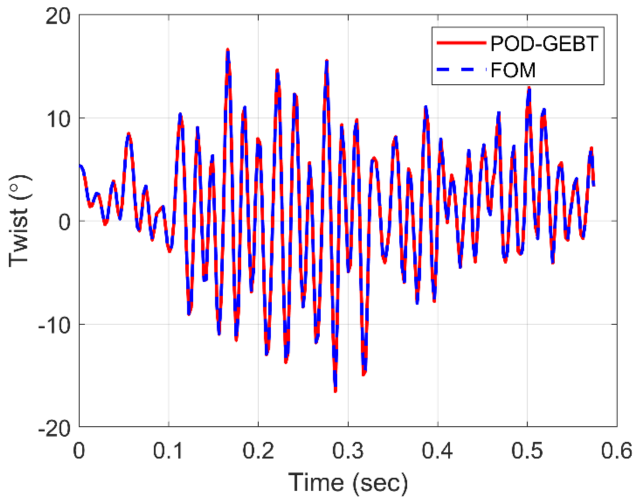

(c) Twist angle except initial twist of HART-II blade

Figure 16: Comparison of tip displacement for dynamic analysis.

Overall, the present ROM provides good agreement when compared to that by FOM. In the case of twist, the FOM showed a significant variation with respect to time, and it is confirmed that the ROM also followed appropriately.

6. CONCLUSIONS

In this study, a ROM is created by applying a POD-based GNAT to mixed variational formulation based geometrically exact beam theory. First, POD-GNAT-GEBT is applied to the aero-structure coupled analysis for the hovering flight of a full-scale hingeless rotor blade. Comparison of the proposed POD-GNAT-GEBT with the FOM, CAMRAD II, DYMORE II, and the experimental data confirmed the accurate prediction of thrust, torque, and performance coefficients. Moreover, the computational efficiency improved significantly, as evidenced by the speed-up factors ranging from 1.69–1.91. For dynamic analysis, the permuted mode is used and confirmed the prediction ability for the unsampled time. Moreover, hyper reduction approach will be employed for improved efficiency of the dynamic analysis.

Author contact:

Haeseong Cho hcho@jbnu.ac.kr

Haedong Kim haedong@sejong.ac.kr, etc.

7. ACKNOWLEDGMENTS

8. REFERENCES

1. Hodges, D. H., and Earl H. D. Nonlinear equations of motion for the elastic bending and torsion of twisted nonuniform rotor blades, No. A-5711. 1974.
2. Hodges, D. H. "A mixed variational formulation based on exact intrinsic equations for dynamics of moving beams." International journal of solids and structures, Vol. 26, (11), 1990, pp. 1253-1273.
3. Bir, G., Chopra, I., and Nguyen, K., "Development of UMARC (University of Maryland advanced rotorcraft code)." AHS, Annual Forum. 1990.
4. Bir, G. "Status of University of Maryland advanced rotorcraft code (UMARC)." Proceedings of the American Helicopter Society Aeromechanics Specialists Conference, San Francisco, California, January 1994.
5. Saberi, H., Khoshlahjeh, M., Ormiston, R. A., and Rutkowski, M. J., "Overview of RCAS and application to advanced rotorcraft problems." American helicopter society 4th decennial specialists' conference on aeromechanics, San Francisco, CA. 2004.
6. Shang, X., Hodges, D. H., and Peters, D. A., "Aeroelastic stability of composite hingeless rotors in hover with finite-state unsteady aerodynamics." Journal of the American Helicopter Society, Vol. 44, (3), 1999, pp. 206-221.
7. Bauchau, O. A., Bottasso, C. L., and Nikishkov, Y. G., "Modeling rotorcraft dynamics with finite element multibody procedures." Mathematical and Computer Modelling, Vol. 33, (10-11), 2001, pp. 1113-1137.
8. Johnson, W., "Technology Drivers in the Development of CAMRAD II." American helicopter society aeromechanics specialists conference, San Francisco, California. 1994.
9. Johnson, W., "Rotorcraft aeromechanics applications of a comprehensive analysis." Heli Japan. Vol. 98. 1998.
10. Sirovich, L., "Turbulence and the dynamics of coherent structures. III. Dynamics and scaling." Quarterly of Applied mathematics, Vol. 45, (3), 1987, pp. 583-590.
11. Amsallem, D., Cortial, J., Carlberg, K., and Farhat, C., "A method for interpolating on manifolds structural dynamics reduced-order models," International Journal for Numerical Methods in Engineering, Vol. 80 ,2009, pp. 1241–1258.
12. LeGresley, P, and Juan A. "Airfoil design optimization using reduced order models based on proper orthogonal decomposition." Fluids 2000 conference and exhibit. 2000.
13. Hall, K. C., Jeffrey P. T., and Hodges, D. H., "Proper orthogonal decomposition technique for transonic unsteady aerodynamic flows." AIAA journal, Vol. 38, (10), 2000, pp. 1853-1862.
14. Lieu, T., Farhat, C. and Lesoinne, M., "Reduced-order fluid/structure modeling of a complete aircraft configuration." Computer methods in applied mechanics and engineering, Vol. 195, (41-43), 2006, pp. 5730-5742.
15. Amsallem, D., and Farhat, C., "Interpolation method for adapting reduced-order models and

application to aeroelasticity." AIAA journal, Vol. 46, (7), 2008, pp. 1803-1813.

16. Amasallem, D., Cortial, J., Carlberg, K., and Farhat, C. , "Towards real-time cfd-based aeroelastic computations using a database of reduced-order models." AIAA Journal, Vol. 48, 2010, pp. 2029-2037.
17. Barrault, M., Maday, Y., Nguyen, N.-C., and Patera, A., “An ‘Empirical Interpolation’ Method: Application to Efficient Reduced-Basis Discretization of Partial Differential Equations,” Comptes Rendus Mathematique, Vol. 339, (9), 2004, pp. 667–672.
18. Chaturantabut, S., and Sorensen, D. C., “Nonlinear Model Reduction via Discrete Empirical Interpolation,” SIAM Journal on Scientific Computing, Vol. 32, (5), 2010, pp. 2737–2764.
19. Farhat, C., Chapman, T., and Avery, P., “Structure–Preserving, Stability, and Accuracy Properties of the Energy–Conserving Sampling and Weighting Method for the Hyper Reduction of Nonlinear Finite Element Dynamic Models,” International Journal for Numerical Methods in Engineering, Vol. 102, (5), 2015, pp. 1077–1110.
20. Carlberg, K., Bou-Mosleh, C., Farhat, C., "Efficient non-linear model reduction via a least-squares Petrov–Galerkin projection and compressive tensor approximations." International Journal for numerical methods in engineering, Vol. 86, (2), 2011, pp. 155-181.
21. Carlberg, K., Farhat, C., Cortial, J., and Amsallem, D., "The GNAT method for nonlinear model reduction: effective implementation and application to computational fluid dynamics and turbulent flows." Journal of Computational Physics, Vol. 242, 2013, pp. 623-647.
22. Im, B., Cho, H., Kee, Y., and Shin, S., “Geometrically exact beam analysis based on the exponential map finite rotations,” International Journal of Aeronautical and Space Sciences, Vol. 21, pp. 153-162.
23. Kim, Y., Kang, S.,Cho, H., and Shin, S., "Improved Nonlinear Analysis of a Propeller Blade Based on Hyper-Reduction." AIAA Journal, 2021, 60(3), pp. 1909-1922.
24. Warmbrodt, W., and Peterson, R. L., Hover test of a full-scale hingeless rotor (No. NASA-TM-85990), 1984.

9. CLASSIFICATION & COPYRIGHT